



Mapping sequences and mineral deposits in poorly exposed lithologies of inaccessible regions in Azad Jammu and Kashmir using SVM with ASTER satellite data

Muhammad Imran¹ · Sultan Ahmad¹ · Amir Sattar¹ · Aqil Tariq²

Received: 5 May 2021 / Accepted: 27 February 2022 / Published online: 15 March 2022
© Saudi Society for Geosciences 2022

Abstract

Exploring minerals, lithological sequences, and geological formations remained challenging in territorial armed conflict and environmentally hazardous zones. Satellite-based remote sensing is appropriate when direct studies are cumbersome due to boundary problems or morphological strains over large inaccessible regions. Therefore, the main objective here is to map different minerals and identify poorly exposed lithology in district Poonch of the Pakistani territory of Azad Jammu and Kashmir, which has a variety of economic deposits and rock sequences. We used support vector machine (SVM) and maximum likelihood classification (MLC) techniques with ASTER and LANDSAT 8 OLI imagery. To validate our results, we conducted ground surveys using GPS, a geological hammer, and a digital camera. Results reveal several mineral deposits, including clay (65%), carbonates (15%), quartz (10%), and ferrous silicate (16%) in the study area. About 45% of minerals show mineral alterations, particularly the clay and quartz minerals. Several formations from the recent Pleistocene age are observed, including the surficial deposits, Kamlial, Murree, Patala, and Abbottabad formations. With ASTER imagery, the accuracy of the SVM classifier is better than MLC to obtain lithological classes with overall kappa statistics (0.86 Versus 0.72), respectively. Overall, the SVM classifier outperformed when used with ASTER imagery. Separate rock samples are tested in the laboratory to validate the minerals mapped from remote sensing. We obtained 90 to 95% accuracy for the mapped minerals. The present study presents a simple approach for mapping poorly exposed lithology in inaccessible regions.

Keywords Exploration and mining · ASTER · Landsat-8 · Support vector machine · Spectral analysis · Alteration rocks · Spatial data mining

Introduction

Geological mapping and mineral exploration remain difficult in poorly exposed lithologies of inaccessible regions. The Hindu Kush Himalaya (HKH) region has long suffered from economic and political marginalization (Pour et al. 2018b; Ahmed et al. 2019). The Azad Jammu and Kashmir (AJK) in the Himalayas is affected by both environmental hazards and border conflicts with lasting impact on geological investigations and other research and development activities (Kelman et al. 2018). Armed conflicts are common in areas adjacent to the line of control (LOC) between Pakistan and India. Consequently, AJK geology remains unidentified because of poorly exposed lithologies in unreachable border areas. Main challenges specific to AJK include fragile and conflict-affected regions, forest covers, remoteness of rock exposures, and rough terrains for geological mapping and sample collection. Several methods use satellite-based

Responsible Editor: Biswajeet Pradhan

✉ Muhammad Imran
imran.igeo@uaar.edu.pk

Sultan Ahmad
sultanalitahir452@gmail.com

Amir Sattar
aamir.dounya@yahoo.com

Aqil Tariq
aqiltariq@whu.edu.cn

¹ Institute of Geoinformation & Earth Observation (IGEO), PMAS Arid Agriculture University, Rawalpindi, Pakistan

² State Key Laboratory of Information Engineering in Surveying, Mapping and Remote Sensing (LIESMARS), Wuhan University, Wuhan, China

remote sensing data for geological mapping of unreachable regions, lithological mapping, structural analysis, and mineral exploration in mountainous areas around the world (Zhang et al. 2016; Pour et al. 2017, 2019a, 2019b; Safari et al. 2018; Pour et al. 2018a, b, c; Saporetti et al. 2019; Bachri et al. 2019).

Remote sensing imagery can identify minerals due to its potential to distinguish minerals interrelated with different natures of mineral forming environments over large, fragile, and conflict-affected areas (Abrams and Yamaguchi 2019). Several studies applied remote sensing data to map mineralogical properties of rocks, mineral assemblages, and weathering characteristics (Bhattacharya et al. 2012; Harris and Grunsky 2015; Pour et al. 2018a, b, c, 2019a, b, c; Wang et al. 2020; Sheikhrhimi et al. 2019). Others used remote sensing to discriminate lithological sequence (Pour and Hashim 2012b; Notesco et al. 2014; Gasmi et al. 2016) and to identify alteration zones (Takodjou et al. 2020). Landsat 8 OLI showed great potential for lithological mapping and discovery of geological structures relative to Landsat 7 and ETM+ (Gutman et al. 2013). The Advanced Spaceborne Thermal Emission and Reflection Radiometer (ASTER) sensor proved appropriate in exploring minerals and lithological sequences at regional scales due to its swath width (scene area 60 km²) and several infrared bands (Abrams and Yamaguchi 2019). For instance, short-wave infrared (SWIR) can discriminate $(Al_2O_3(SiO_2)_2(H_2O)_2)$, and Illite, CO_3 . Thermal bands can map carbonate and quartz based on their silica content (Guha et al. 2018; Rajan and Mayappan 2019).

Various types of rocks reflect different wavelengths of electromagnetic energy, which is the basis to identify spectral characteristics of the rock mineralogy, and, thus, to map complicated class distributions from remote sensing data. To this, several indices or band ratios tend to distinguish lithological units, e.g., band ratios 3/1 and 5/4 of Landsat ETM+ highlights iron oxide (Fuentes et al. 2020), ASTER thermal band ratios 14/12 and 13/14 emphasize silicate and carbonate minerals (Pour and Hashim 2012b). The band ratios along with image transformation techniques (e.g., PCA, ICA, MNF) enhanced present geological maps to detect groups of minerals, e.g., CO_3 and Mg – O – H (Askari et al. 2018; Takodjou et al. 2020). Alternatively, the similarity-based methods tend to match image spectra to previously measured spectral profiles (Bolouki et al. 2020). The probabilistic approaches compute the probability of similarity between a pixel spectrum and the reference spectrum (Sheikhrhimi et al. 2019), ranging from zero to a user-defined threshold. Similarly, the fuzzy-logic theory is applied to fuse the most informative thematic layers (Sekandari et al. 2020). However, these threshold-dependent similarity-based approaches have limitations of discriminating different lithological units for scenes with varying sizes and thresholds.

Statistical methods use summary statistics from classes of image pixels (Bachri et al. 2019). Such spectrum-based approaches tend to classify different lithological features in the study area through deterministically or probabilistically differentiating the spectral information (Bachri et al. 2019). Commonly used statistical classification methods for mapping sequences and mineral deposits are minimum distance and maximum likelihood classification (Pour et al. 2019b). Minimum distance utilizes the mean of the training spectral profiles for separating classes. The maximum likelihood (ML) uses both the mean and the covariance matrix. Thus, it exploits the information contained in a data set without the assumption of data distribution. The statistical methods have a clear advantage of investigating poorly exposed lithologies due to limited field data in inaccessible regions. Also, statistical learning approaches for data mining can better learn and approximate complex non-linear mapping in those regions. Support vector machines (SVM) can model unknown multivariate distributions that capture complex and multistage geological events (Othman and Gloaguen 2017). Moreover, it is less sensitive to the number of samples compared to other machine learning models (Kumar et al. 2020).

The main objective of this study is to apply SVM for supervised non-parametric classification of RS data and compare the results with previously applied ML for mapping poorly exposed lithologies of inaccessible regions in AJK using Landsat-8 and ASTER reflective and thermal bands. Moreover, we validated the research output through the field data obtained by testing the separate rock samples in the laboratory.

The research output will establish a simple satellite-based approach for not only mapping geological formations at regional scales but also identifying minerals and lithological sequences in the LOC-border of AJK region and other fragile and conflict-affected, forest-covered, and difficult terrains around the world, having scarce geological information.

Geological setting of the study area

The district of Poonch ($33^{\circ}46'N;74^{\circ}5'E$) is adjacent to the line of control, Azad Jammu and Kashmir (AJK) (see Fig. 1). The study area is one of the populated regions of the Himalayan Pir Panjal, which is a humid sub-tropical mountainous range of tough terrain. It contains rocks from the geological periods between the recent and Pleistocene. Figure 1b–c show geological formations in different regions of the study area. The surficial deposits are mainly composed of boulders, cobbles, and pebbles of the recent to sub-recent ages (Lydekker 1876). While the Kamlial Formation constitutes sandstone, intra-formational conglomerates, and clay of the Early to Middle Miocene Epoch. The Murree Formation of the early Miocene Epoch is composed of clays, shales,

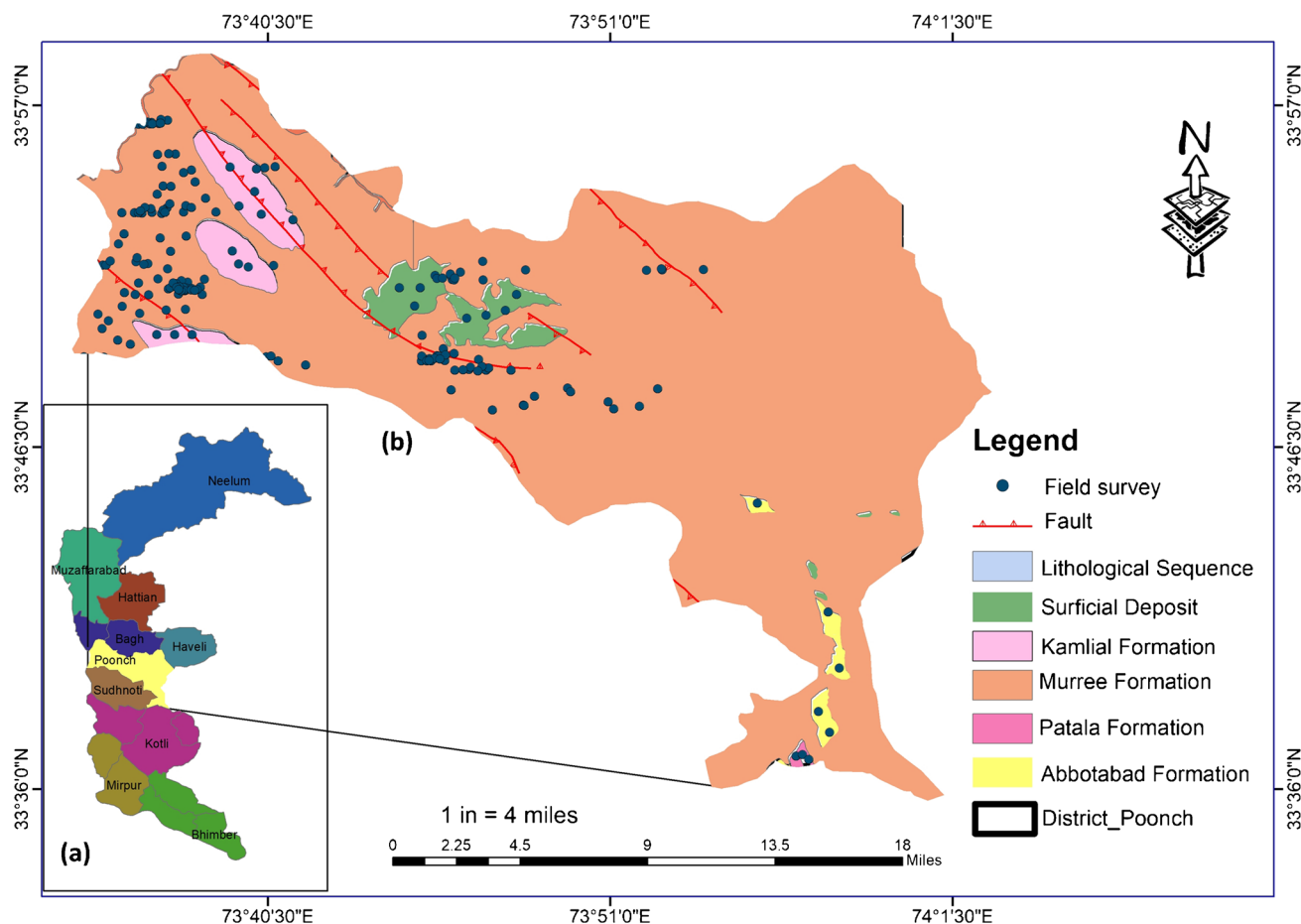


Fig. 1 Azad Jammu and Kashmir (AJK) region (a); map of district Poonch adapted from Land Use Planing & Development Department, AJK Government (<https://pndajk.gov.pk/>) showing geology of the study area adapted from topo sheets of formations from the Survey of Pakistan (b)

and medium-grain-red and purple-red sandstone (Pilgrim 1937). The Patala Formation of the Late Paleocene age is mainly composed of shales with inter-bedded limestone. The Abbottabad Formation from Miocene-Pleistocene consists of dolomitic limestone, cherty dolomite, and chert bands (Ashraf et al. 1983). The Nagri Formation from the late Miocene consists of greenish-gray to light-gray, medium to coarse-grained sandstone (60%) that alternate with 40% clays.

Materials and methods

Ground surveying and microscopic analyses

For training and validation purposes in this study, we obtained GPS-based ground observations of minerals and formations through random sampling. We marked the sampling points through the topo sheets of geological formations obtained from the Survey of Pakistan. The topo sheets include 43 (K-2, K-1, G-13, G-9, and G-14B). The ground

surveys were conducted between 20 February 2019 to 27 February 2019 using GPS total station, a geological hammer, and a digital camera. In total, 200 locations were sampled in the study area (see Fig. 1).

Thin sections of the rock samples taken from different locations were examined under a petrographic microscope to identify minerals in the study area. The visual acuity is helpful to determine the relative abundance of a mineral grain and its composition and texture. Compared to the X-ray diffraction (XRD) technique, petrography is more reliable for determining the mineralogical composition of rocks through textural analyses (Amaral et al. 2006). Therefore, the petrography analysis supports the validation of mineral assemblage mapped through remote sensing techniques (such as band ratios) applied in this study.

Satellite remote sensing

For geological mapping over large areas, we obtained cloud-free level-1B ASTER data for November 18, 2007, and level 1 T (L1 T) L8 OLI data acquired on July 10,

2018, and December 1, 2018 (see Table 1 for details). We geo-referenced the imagery and applied radiometric calibration with band interleaved by lines format. We carefully obtained and pre-processed the imagery through the following considerations:

- The sun's zenith angle should be almost in nadir for the area to reduce the cast shadows.
- We applied an atmospheric correction to ASTER and OLI/Landsat-8 images through setting sensor altitude, the sun's zenith angle, sensor type, elevation, and multispectral settings in the FLASH (Fast Line of Sight Atmospheric Analysis of Hypercubes) module. It eliminates the effects of water vapors and clouds and converts the digital counts to surface reflectance.
- The spectra from ASTER and Landsat should be cross-checked with ASTER spectral libraries. We applied cross-track illumination correction to ASTER images to remove the energy overspill effect from band 4 to bands 5–9 (Ge et al. 2018).

Image processing for lithological mapping

Geological mapping through remote sensing generally aims to identify types and geologic structures of various lithologic units of exposed rocks over larger areas through analyzing the imagery from one or more sensors. To do so, we used three different image processing methods: maximum likelihood classification, support vector machine, band ratios with Landsat OLI and ASTER data, laboratory spectral reflectance measurements of rock samples, and field observations. We applied these methods with the following experimental settings.

Band ratios

ASTER data contains higher spectral and spatial resolution in the VNIR to SWIR range than other commonly used multispectral data. Therefore, OLI and ASTER band ratios can be appropriate to analyze several visual characteristics (e.g., texture, color, and other visual features) of minerals and materials that can be unseen in raw bands (Ibrahim et al. 2016). Moreover, band ratios increase image contrast that improves the extraction of lithology through remote sensing. In this study, we calculated the band ratio $(7 + 9)/8$ for mapping carbonates and altered rocks (limestone

Table 1 Spatial, spectral, radiometric resolution of near infrared (NIR), very near infrared (VNIR), short-wave infrared (SWIR), and thermal infrared (TIR) bands of LANDSAT 8 OLI data and ASTER imagery

Satellite imagery	Product	Spectral bands	Spectral range (μ m)	Spatial resolution (m)	Radiometric resolution
ASTER T1	VNIR	1	0.5–0.60	15	8
		2	0.63–0.69		
		3 N	0.78–0.86		
		3B	0.78–0.86		
	SWIR	4	1.60–1.70	30	8
		5	2.145–2.185		
		6	2.185–2.225		
		7	2.235–2.85		
		8	2.295–2.365		
		9	2.360–2.430		
		10	8.125–8.475		
	11	8.475–8.825			
	12	8.925–9.275			
	13	10.25–10.95			
Landsat-8 OLI		Band 1 – coastal aerosol	0.435–0.451	30	12
		Band 2 – blue	0.452–0.512		
		Band 3 – green	0.533–0.590		
		Band 4 – red	0.636–0.673		
		Band 5 – NIR	0.851–0.879		
		Band 6 – SWIR-1	1.566–1.651		
		Band 7 – SWIR-2	2.107–2.294		

CaCO₃ and dolomite CaMg(CO₃)₂, the band ratio (7/6) for muscovite KAl₂(AlSi₃O₁₀)(OH, F)₂ and muscovite mica (also known as mica, isinglass, and potash mica) (KF)₂(Al₂O₃)₃(SiO₂)₆(H₂O), the band ratio (7/5) for clay mineral kaolinite (Al₂O₃(SiO₂)₂(H₂O)₂), the band ratio (4/5) for laterite rock type 4H3. – 2H3, the band ratio (5/4) for ferrous silicate SiO₂, the band ratio (13/12) for quartz FeSiO₃, and the band ratio (4/5) for mapping alteration rocks. We validated the identified lithological units through band ratios by location-based ground surveys.

Maximum likelihood classification

Maximum likelihood classification (MLC) differentiates lithological classes by measuring a multivariate probability density function with mean and the covariance matrix, where the unknown pixels are assigned to classes with the highest probability of belonging (Pedroni 2003; Pour et al. 2019b).

$$P\left(\frac{X_i}{i}\right) = \frac{1}{(2\pi)^{(n/2)}V^{(1/2)}} \exp\left[-1/2(x_k - \mu_i)^r (V_i)^{-1}(x_k - \mu_i)\right] \tag{1}$$

where $P\left(\frac{X_i}{i}\right)$ is the probability density function for a pixel x_k as a member of class I , n is the number of wavebands, x_k is the data vector for the pixel in all wavebands, μ_i is the mean vector for class I over all pixels, and V_i^{-1} is the variance–covariance matrix for class i . The term $(x_k - \mu_i)^r (V_i)^{-1}(x_k - \mu_i)$ is the Mahalanobis distance between the pixel and the centroid of class I .

The MLC algorithm assumes normally distributed samples in the study area. With the satisfied normality assumption, Ge et al. (2018) showed a higher overall accuracy of the classification using MLC compared to that of SVM. The optimal properties may not apply for MLC with a small sample size, resulting in highly biased model estimates. In this study, we used a single threshold value with the 1.0 data scale factor.

Support vector machine

Support vector machine (SVM) classifies the data by transforming the original training data to a higher-dimensional space (Vapnik 1995; Othman and Gloaguen 2017; Zuo 2017). To do so, first, it constructs a hyperplane in the higher-dimensional space with a maximum distance to the nearest support vectors (i.e., samples). Next, it finds an optimal separator hyperplane that maximizes the distance between the lithological classes (margins), such that for a given set of training examples, $\{(x_i, \mu_i)\}_{i=1}^n$, for a pixel x_i and Kernel function V , each $\mu_i = \{-1, +1\}$ can be assigned

to one of two lithological classes. An SVM object function is used to solve the optimization problem as (Liu et al. 2017):

$$\max_{\alpha} \left\{ \sum_{i=1}^n \alpha_i + \sum_{i,j=1}^n \alpha_i \alpha_j \mu_i \mu_j V(x_i, x_j) \right\} \tag{2}$$

$$s.t. \tag{3}$$

$$0 \leq \alpha_i \leq C \tag{4}$$

$$\sum_{i=1}^n \alpha_i \mu_i = 0 \tag{5}$$

where α s are the Lagrange coefficients and C is a constant used to penalize the training errors of the samples. We applied SVM for the geological mapping in this study because of the following advantages,

1. Compared to traditional methods, the accuracy of the SVM classification is higher when the dimensionality of data is high and the training data set is small (Othman and Gloaguen 2017). It is a common problem in remote sensing applications for lithological mapping.
2. SVM can define non-linear decision boundaries in high-dimensional feature space by solving the quadratic optimization problem (Eq. 1) (Bachri et al 2019).
3. SVM can better differentiate mid-sedimentary rocks during the lithological classifications compared to other machine learning methods like self-organizing maps, neural networks, and genetic algorithms (Sahoo and Jha 2017).

Like other machine learning approaches, SVM can be sensitive to over-fitting the kernel selection criterion (Liu et al. 2017). Therefore, the performance of an SVM model depends on the selection of regularization parameters α s and the form of the kernel function $V(x_i, x_j)$, such as linear, polynomial, sigmoid, and radial basis functions (RBF) (Zuo 2017). The RBF is commonly used in lithological mapping using remote sensing images because of its efficient interpolation capabilities (Bachri et al 2019). In this study, we applied SVM on the training data set using the radial kernel function. Here, the two vital parameters are the gamma kernel width and the penalty parameter that influence the RBF-SVM performance. A high value for penalty parameters results in training errors, while a small penalty value generates a higher margin and, thus, increases the number of training errors (Kumar et al 2020). A penalty value of 100 resulted in optimal RBF-SVM performance in the classification of remote sensing data (Yang 2011; Bachri et al 2019).

In this study, we set the penalty parameter to 100, and the gamma parameter in the kernel function was the inverse of the ASTER band numbers, i.e., 0.071.

Accuracy assessment

We observed a total of 200 geological locations for the accuracy assessment of both MLC and SVM classifiers. The ground survey data were randomly split into two subsets: a subset of 70% rocks samples for training the lithological classifier; and 30% reference samples to assess accuracies. We calculated the confusion matrix to evaluate the overall classification accuracy of the remotely sensed data, user and producer accuracy, and kappa coefficient (Congalton 1991; Lillesand et al. 2014).

Results

Ground surveys, microscopic analyses, and observed structures

Figure 2a–h show sampled rocks and structures of flute casts (a), calcareous shale (b), fracture filled with calcite (c), conglomeratic bed (d), limestone clast (e), mud crakes (f), siltstone clast (g), and volcanic clast (h) in the study area.

Results of petrographic analysis of sampled units (see Fig. 3a–h) show the mineral deposits of muscovite,

muscovite mica, quartz, alteration minerals, sutured ferrous silicate, biotite schist, hematite concretions, altered ferrous silicate, and deformed muscovite. The secondary sedimentary structures observed in the study area include the carbonate concretions from shale beds whose chemical composition is of calcite nature. These concretions are a few centimeters in size with conical, spherical, and disc shapes.

Band ratios

Multiple band ratios are processed for increasing image contrast for the extraction of lithology. Results are validated from the microscopic laboratory analysis of the study area. Figure 4a shows quartz (FeSiO_3) is mainly present in Banjosa, Marchkot, and Khali Dharman areas in the Murree Formation. Quartz prevents the flow of carbon from the steel. Therefore, it is widely used in industries as a deoxidizer. The total area of quartz calculated in the study area is 143 km². Figure 4b and Fig. 1b–c indicate that the clay mineral kaolinite ($\text{Al}_2\text{O}_3(\text{SiO}_2)_2(\text{H}_2\text{O})_2$) is heavily present in Rawalakot and Hajira areas of the Kamliyal Formation and Murree Formation. Kaolinites are primarily layered silicates formed by feldspar (another clay mineral) weathering. It is water-insoluble and dark while its concentration is 2.65g/cm³. The total area of kaolinites is projected to be 400 km² in the study area.

Figure 4c and Fig. 1b–c show muscovite mica presence in the Abbottabad Formation, surficial deposits, and Murree

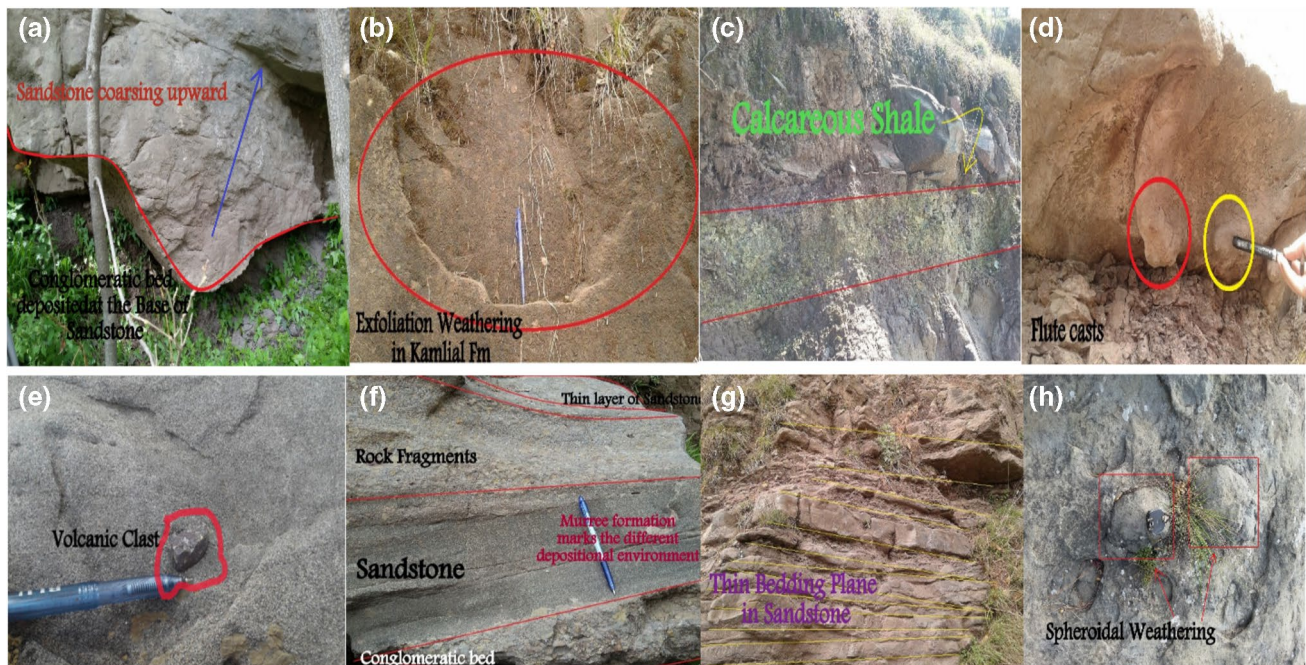


Fig. 2 Sampled rocks and structures details of flute casts (a), calcareous shale (b), fracture filled with calcite (c), conglomeratic bed (d), limestone clast (e), mud crakes (f), siltstone clast (g), and volcanic clast (h) in Poonch, Azad Jammu and Kashmir (AJK)

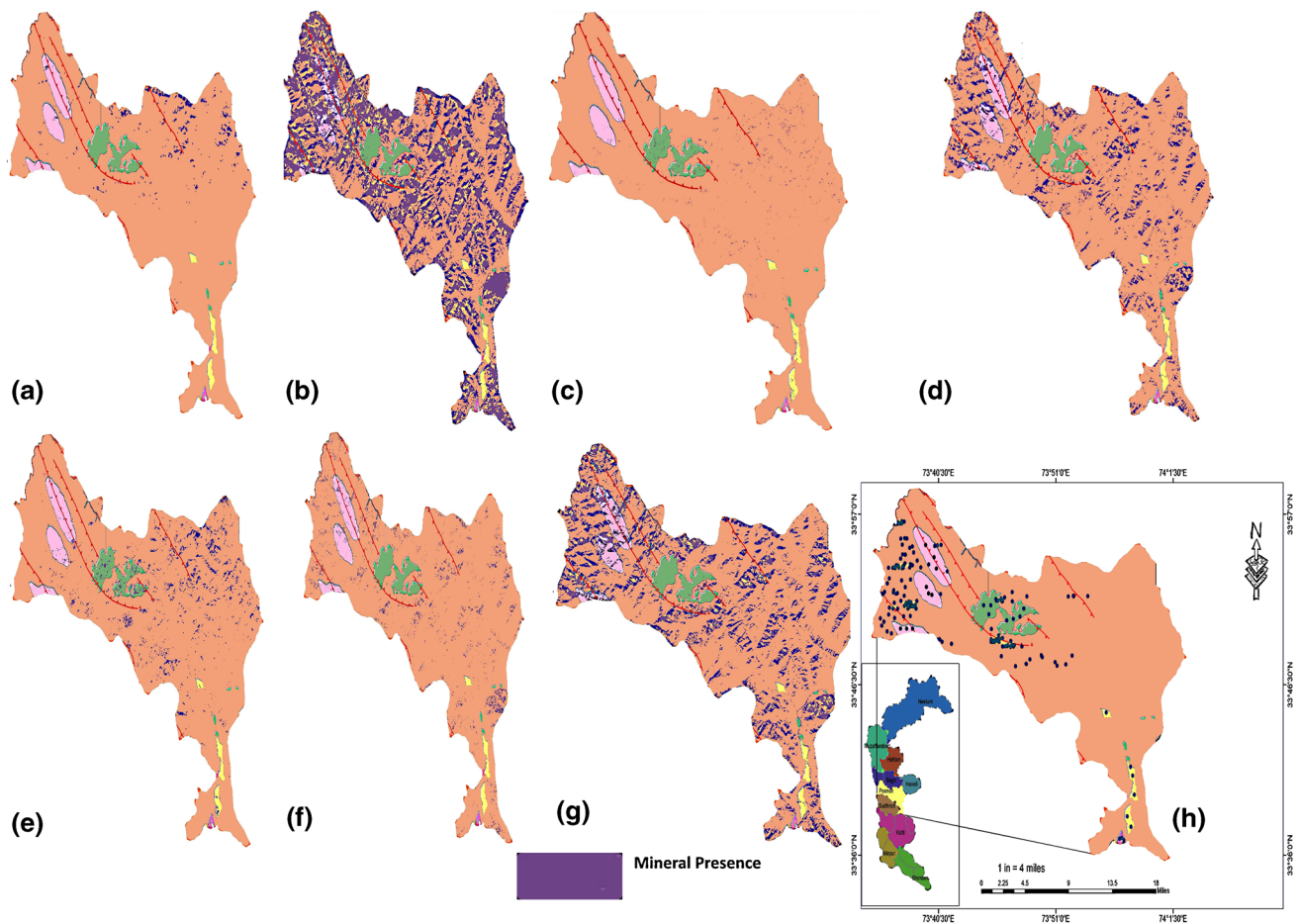


Fig. 3 Microscopic analysis confirms the presence of muscovite and muscovite mica (a), quartz FeSiO_3 (b), alteration minerals (c), carbonates and alteration rocks (limestone CaCO_3 , dolomite

$\text{CaMg}(\text{CO}_3)_2$ (d), biotite schist (e), hematite concretions (f), altered ferrous silicate (g), and deformed muscovite (h)

Formation in Khali Dharman, Tulipir, and Tahri areas, which could be possibly due to the presence of ophiolites complexes metamorphic rocks. In the study area, muscovite is generally found in the associated form with sericite. The total area of muscovite is calculated to be 18 km^2 . Figure 4d indicates the presence of laterite $4\text{H}_3 - 2\text{H}_3$ mainly in Kamliyal Formation and Murree Formation. Typical laterite is fragile and clay-like, with higher ratios in the northern and southern parts of the study area, whereas lower ratios in the central part. The iron oxide contains goethite HFeO_2 crystals, lepidocrocite $\text{FeO}(\text{OH})$, and hematite Fe_2O_3 . It comprises the most common and accessible titanium oxides and aluminum hydrated oxides $4\text{H}_3 - 2\text{H}_3 \cdot 3\text{H}_2\text{O}$, which is primarily reddish claystone due to weathering of iron-rich minerals in wet or humid environments. Its total area is estimated to be 182 km^2 .

Figure 4e and Fig. 1b–c indicate the presence of ferrous silicate (FeSiO_3) in the Murree Formation in the northeastern parts (i.e., Banjosa, Marchkot, and Khali Dharman). The total area of ferrous silicate in the study area is 143 km^2 .

Figure 4f shows the presence of carbonates and alteration rocks limestone CaCO_3 and dolomite $\text{CaMg}(\text{CO}_3)_2$ mainly in the Kamliyal and Murree formations. They are highly present in Bhangiun, Tain Dhalkot, Bhalgran, Parat, and adjacent areas of Tehsil Rawalakot, and in Dharmasala, Tattapani, and Dara of Tehsil Hajira. Overall, the northern part is high in carbonates comprising a total area of 134 km^2 . These carbonates are important components of calcareous, dolomite, and siderite rocks, including CaCO_3 , $\text{CaMg}(\text{CO}_3)_2$, and FeCO_3 . Figure 4g shows that altered ferrous silicate is excessively present in the northern part (i.e., Bhangiun, Jandali, and Pachiot) and the southern part (i.e., Dharmasal and Sehra). Clay minerals and SiO_2 rich rocks show excessive alteration. The calculated area of the altered rocks in the study area is 392 km^2 .

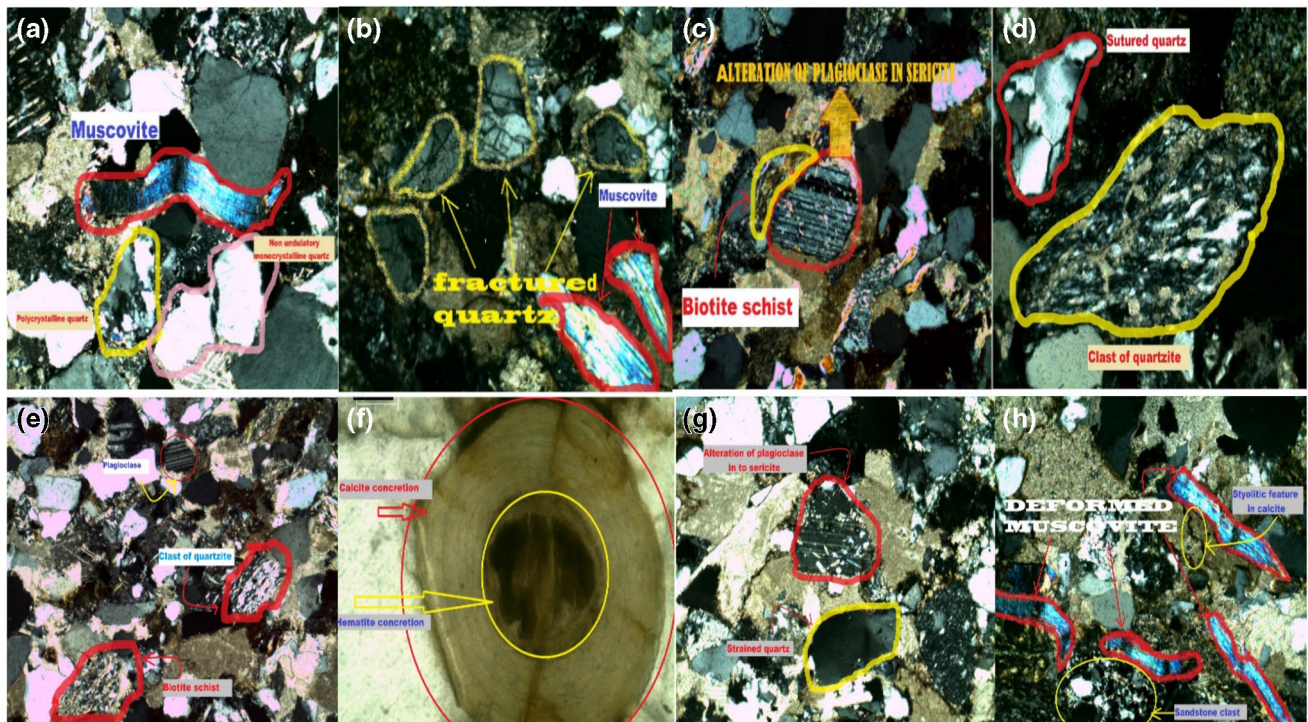


Fig. 4 Multiple band ratios showing the quartz FeSiO_3 (a), clay mineral kaolinite $(\text{Al}_2\text{O}_3(\text{SiO}_2)_2(\text{H}_2\text{O})_2)$ (b), muscovite (mica) (c), laterite $4\text{H}_3 - 2\text{H}_3$ (d), ferrous silicate FeSiO_3 (e), dolomite

$\text{CaMg}(\text{CO}_3)_2$ (f), and altered ferrous silicate (g) in Poonch, Azad Jammu and Kashmir (AJK)

Classifier performance for the identification of lithological formations through ASTER and LANDSAT 8 OLI imagery

Figure 5a shows the results of the MLC classification of LANDSAT 8 OLI imagery. It indicates various geological formations present in the study area. The geological formations identified from ML classification on the LANDSAT 8 OLI data show some variations with the geological map of the survey of Pakistan (SOP) (see Fig. 1). The Murree Formation is dominated, followed by the Kamlial, Patala, and Abbottabad formations. Similar patterns of formations appear in the SVM classified map through LANDSAT 8 OLI imagery (Fig. 5b). However, the surficial deposits are more dominant, particularly in the tail of the study area on the south. Whereas, in the same area, the Patala Formation, which largely appeared in the ML classification map, is missing in the SVM classification map. Comparing it with the SOP formation map in Fig. 1 and accuracy statistics in Table 2, the identification of the Patala Formation improved with ASTER imagery. It is further indicated by increased user accuracy from less than 67.51 to 90% accuracy in all of the two classification methods (i.e., MLC in Fig. 5b & SVM in Fig. 5d).

The Abbottabad Formation is absent in the lithological maps (Fig. 5c–d), which we obtained through MLC and

SVM classifiers with ASTER data. However, it is present in the SVM classified map from LANDSAT 8 OLI imagery (Fig. 5b). On the other hand, the Patala Formation has high omission errors, i.e., the producer's accuracy is low, and there is a probability that reference samples for this formation are wrongly classified.

Classifier performance for the identification of minerals through ASTER imagery

Figure 6 shows maps of lithological sequences in the district Poonch obtained through ASTER data with MLC Fig. 6a and SVM Fig. 6b classifiers. Both classifiers predominantly identify the presence of alteration rocks (limestone CaCO_3 and dolomite $\text{CaMg}(\text{CO}_3)_2$, followed by the laterite $4\text{H}_3 - 2\text{H}_3$, and clay mineral kaolinite $(\text{Al}_2\text{O}_3(\text{SiO}_2)_2(\text{H}_2\text{O})_2)$. The quartz FeSiO_3 is present in the north of the study area. Compared to MLC, the SVM classifier better identified the presence of muscovite $\text{KAl}_2(\text{AlSi}_3\text{O}_{10})(\text{OH}, \text{F})_2$ in the study area. The mineral maps indicate the deposition of shale and sedimentary rocks. With ASTER imagery, the accuracy of the SVM classifier is better than MLC to classify the lithological sequences with overall kappa statistics (0.93 Versus 0.61) and overall accuracy (95.2% versus 70.7%), respectively.

Fig. 5 Classified lithological sequences in the district Poonch obtained through LANDSAT 8 OLI data with maximum likelihood classification (MLC) (a), support vector machine (SVM) classification (b); and, through ASTER data with MLC (c), and SVM (d)

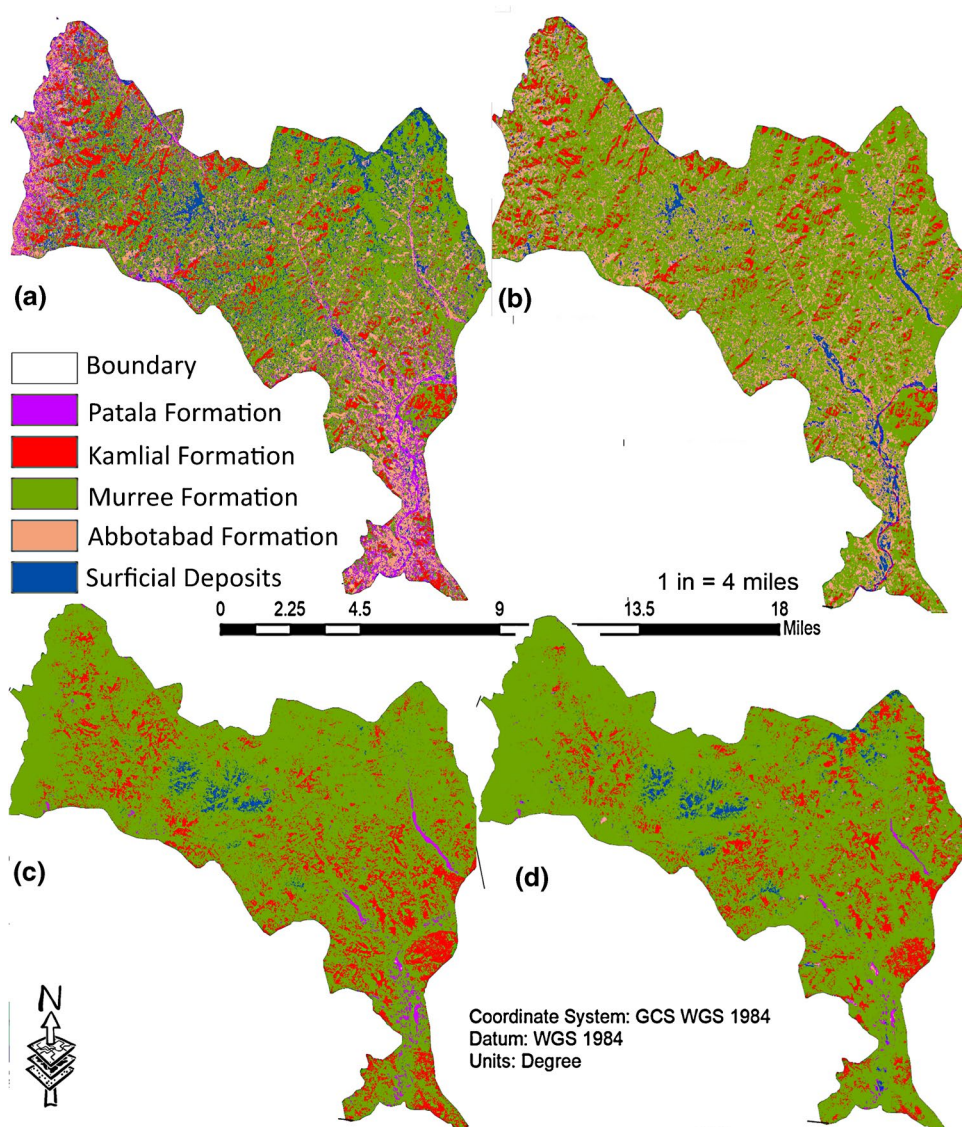
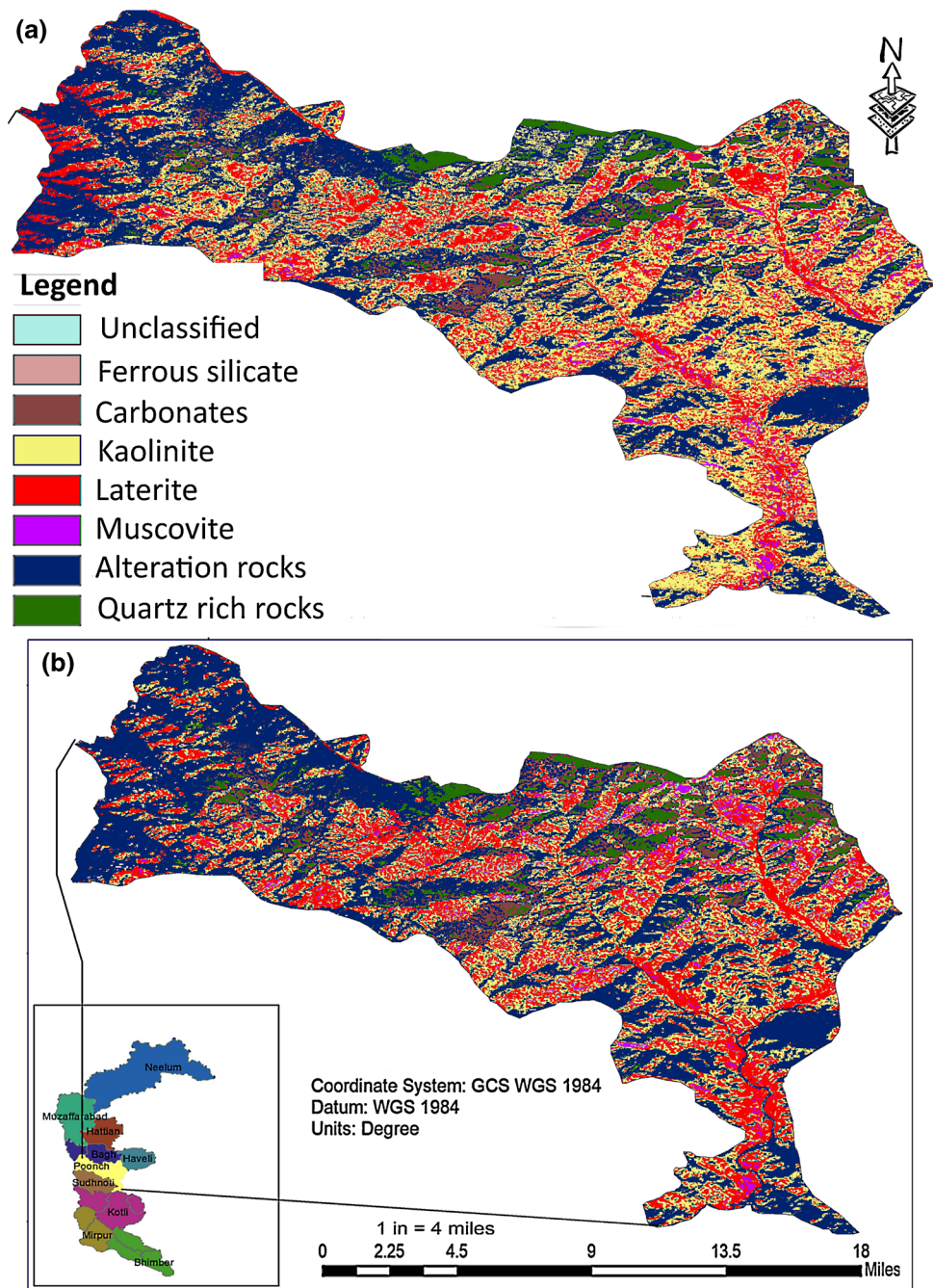


Table 2 Summary of accuracy (%) and Kappa statistics of lithological classes obtained from LANDSAT 8 OLI data and ASTER imagery classifications through maximum likelihood classification (MLC) and support vector machine (SVM)

Class	LANDSAT 8 OLI				ASTER			
	MLC		SVM		MLC		SVM	
	Producer accuracy (%)	User accuracy (%)	Producer accuracy (%)	User accuracy (%)	Producer accuracy (%)	User accuracy (%)	Producer accuracy (%)	User accuracy (%)
Murree	78.84	98.72	96.41	90.88	95.74	99.82	99.38	99.09
Abbottabad	79.15	71.23	63.71	72.34	98.10	100.0	89.52	87.04
Kamliial	84.11	37.74	32.78	66.44	96.40	53.51	83.68	88.58
Patala	92.28	67.51	0.00	0.00	100.0	97.33	85.62	91.24
Surficial	91.30	10.82	66.41	67.45	100.0	79.27	88.46	87.79
Overall accuracy	56.51%		67.27%		95.83%		98.48%	
Kappa statistics	0.51 (Weak)		0.63 (Moderate)		0.72 (Moderate)		0.86 (Strong)	

The overall accuracy greater than 90% shows high classification accuracy, i.e., more than 90% of assigned pixels are correctly assigned. The Kappa coefficients show weak to strong level of agreement between classified and reference classes

Fig. 6 Mineral map of the district Poonch obtained through ASTER data with maximum likelihood classification (MLC) (a), with support vector machine (SVM) classification (b) classifiers



Lithological classification and accuracy assessment

Table 2 shows a summary of accuracy (%) and Kappa statistics of lithological classes obtained from LANDSAT 8 OLI data and ASTER imagery classifications through MLC and SVM.

For the MLC classification using Landsat 8 OLI imagery, the producer accuracy of Muree, Abbottabad, Kamliyal, Patala, and surficial formations is 78.84%, 79.15%, 84.11%, 92.28%, and 91.30%, whereas user

accuracy is 98.72%, 71.23%, 37.74%, 67.51%, and 10.82%, respectively. For the MLC classification using ASTER imagery, the producer accuracy of Muree, Abbottabad, Kamliyal, Patala, and surficial formations is 95.74%, 98.10%, 96.40%, 100.00%, and 100.00%, whereas user accuracy is 99.82%, 100.00%, 53.51%, 97.33%, and 79.27%, respectively. The MLC performance improved from overall kappa and accuracy statistics are 0.51 and 56.51% with Landsat imagery to 0.63 and 67.27% with ASTER data, respectively.

For the SVM classification using Landsat 8 OLI imagery, the producer accuracy for Muree, Abbottabad, Kamlial, Patala, and surficial formations are 96.41%, 63.71%, 32.78%, 0.00%, and 66.41%, and user accuracy is 90.88%, 72.34%, 66.44%, 0.00%, and 67.45%, respectively. For the SVM classification using ASTER imagery, the producer accuracy of Muree, Abbottabad, Kamlial, Patala, and surficial formations is 99.38%, 89.52%, 83.62%, 85.62%, and 88.46%, and the user accuracy is 99.09%, 87.04%, 88.58%, 91.24%, and 87.79%, respectively. The SVM performance is improved with overall kappa and accuracy statistics equal to 0.63 and 67.27% and 0.86 and 98.48% with Landsat and ASTER imagery, respectively.

Discussions

We used MLC and SVM with ASTER and LANDSAT 8 OLI imagery to map minerals in the regional scale of the district Poonch of Azad Jammu and Kashmir (AJK). Field surveys conducted during 20–27 February 2019 used the GPS, geological hammer, and digital camera. The petrographic analyses of field observations validated the mineral mapping from remotely sensed data.

The microscopic analyses show several primary sedimentary structures in the study area. The interbed structures (or pre-depositional) generally consist of erosion features. Under this category, we observed groove marks in the sandstone of the Murree Formation in the study area. The intra-bed structures (or syndepositional) consist of bedding in sedimentary rocks. Under this category, the sandstone beds range from 1 cm to a few meters in the study area. The Murree Formation bedding sandstone and laminations in sediments of shale are distinct. The asymmetrical ripple marks are observed in Nagri Formation sandstone (middle Siwaliks). In pebble imbrications, the clasts of variable size and composition in the Dhok Pathan Formation (upper Siwaliks) sandy matrix stacked against each other. The clasts are geared toward the current flow. The pebble imbrications from Jessa Pir conglomerates are reported in the study area.

The work of Kumar et al. (2020) has revealed that SVM outperforms other machine learning models irrespective of the input dataset used in the classification. In this study, we used the ASTER and Landsat data sets to identify lithological formations. To this, the performance of the SVM classifier appears better when used with ASTER imagery. However, in the case of SVM used with Landsat OLI imagery, the classifier could not perform well in deriving accurate and reliable identification of the Patala category. Contrarily, the Abbottabad Formation is missing in the maps prepared through classifying ASTER imagery by MLC and SVM. However, it appears in the map obtained through the SVM classifier with LANDSAT 8 OLI imager. It may be due to

some spectral mixing associated with a specific alteration mapping that may better be differentiated with different imagery (Sekandari et al. 2020). Therefore, fusing the most useful thematic layers obtained from several sensors may produce more informative mineral maps at regional scales (Takodjou et al. 2020).

The work of Sheikhrasimi et al. (2019) found geochemical anomaly locations mostly surrounded by muscovite/illite mineral groups. It may be because the similarity-based methods SAM and SID may not well-matched the ASTER VNIR/SWIR spectral bands to the reference spectra of selected end-member minerals. Here, the SVM classifier better identified the presence of muscovite $KAl_2(AlSi_3O_{10})(OH, F)_2$ in the study area. Thus, SVM can better discriminate different lithological units for scenes with varying sizes and thresholds.

The Band Ratios Matrix Transformation (BRMT) developed by Askari et al. (2018) showed promising results to discriminate the boundary of sedimentary rock formations using ASTER VNIR and SWIR bands. The BRMT approach well identified the carbonate, quartz, and Fe, Al, Mg –OH bearing-altered minerals such as mica, laterite, and clay mineral kaolinite. In this study, SVM predominantly identified the presence of limestone, and dolomite, followed by laterite and kaolinite. However, since the SVM approach is less sensitive to the number of samples (Kumar et al. 2020), it can be a better candidate for mapping sequences and mineral deposits in poorly exposed lithologies of inaccessible regions in Azad Jammu and Kashmir. Future studies can compare the BRMT and SVM approaches for those areas. Furthermore, the SVM applications need to investigate the potential of hyperspectral imagery for more precise and accurate mineral explorations over regional scales.

Conclusion

The new information extracted from ASTER specialized band ratios, MLC, and SVM revealed several potential ferrous silicates, dolomite, and limestone zones in the district Poonch of Azad Jammu and Kashmir (AJK). We observed a total area of 143 km² for ferrous silicate, 392 km² for altered dolomite rocks, and 182 km² for both titanium oxides and aluminum hydrated oxides. Overall, the northern part of the study area is high in limestone, comprising a total area of 134 km².

With ASTER imagery, the accuracy of the SVM classifier is better than MLC to obtain lithological classes with overall kappa statistics (0.86 Versus 0.72) and overall accuracy (98.48% versus 95.83%), respectively. With Landsat OLI imagery, once again, the accuracy of the SVM classifier is better than MLC to obtain lithological classes with overall kappa statistics (0.63 Versus 0.51) and

overall accuracy (67.27% versus 56.51%), respectively. Compared to MLC, the SVM classifier better identified the presence of muscovite in the study area. Through the field analysis and laboratory work, we confirm 90–95% accuracy of SVM with ASTER imagery to identify minerals and lithological sequences. Overall, the SVM classifier outperformed when used with ASTER imagery.

Declarations

Conflict of interest The authors declare that they have no competing interests.

References

- Abrams M, Yamaguchi Y (2019) Twenty years of ASTER contributions to lithologic mapping and mineral exploration. *Remote Sens* 11(11):1394
- Ahmed B, Sammonds P, Saville NM et al (2019) Indigenous mountain people's risk perception to environmental hazards in border conflict areas. *Int J Disast Risk Re* 35:101063
- Amaral PM, Fernandes JC, Rosa LG (2006) A comparison between X-ray diffraction and petrography techniques used to determine the mineralogical composition of granite and comparable hard rocks. In *Mater Sci Forum* 514:1628–32 (Trans Tech Publ)
- Ashraf M, Chaudhry MN, Qureshi KA (1983) Stratigraphy of Kotli area of Azad Kashmir and its correlation with standard type areas of Pakistan. *Kashmir J Geol* 1(1):19–29
- Askari G, Pour AB, Pradhan B et al (2018) Band Ratios Matrix Transformation (BRMT): a sedimentary lithology mapping approach using ASTER satellite sensor. *Sensors* 18(10):3213
- Bachri I, Hakdaoui M, Raji M, Teodoro AC et al (2019) Machine learning algorithms for automatic lithological mapping using remote sensing data: a case study from Souk Arbaa Sahel, Sidi Ifni Inlier, Western Anti-Atlas. *Morocco Isprs Int J Geo-Inf* 8(6):248
- Bhattacharya S, Majumdar TJ, Rajawat AS et al (2012) Utilization of Hyperion data over Dongargarh, India, for mapping altered/ weathered and clay minerals along with field spectral measurements. *Int J Remote Sens* 33(17):5438–5450
- Bolouki SM, Ramazi HR, Maghsoudi A et al (2020) A remote sensing-based application of Bayesian networks for epithermal gold potential mapping in Ahar-Arasbaran area. *Nw Iran Remote Sens* 12(1):105
- Congalton RG (1991) A review of assessing the accuracy of classifications of remotely sensed data. *Remote Sens Environ* 37(1):35–46
- Fuentes I, Padarian J, Iwanaga T et al (2020) 3D lithological mapping of borehole descriptions using word embeddings. *Comput Geosci* 141:104516
- Gasmi A, Gomez C, Zouari H et al (2016) PCA and SVM as geocomputational methods for geological mapping in the southern of Tunisia, using ASTER remote sensing data set. *Arab J Geosci* 9(20):753
- Ge W, Cheng Q, Tang Y et al (2018) Lithological classification using Sentinel-2A data in the Shibanjing ophiolite complex in inner Mongolia. *China Remote Sens* 10(4):638
- Guha S, Govil H, Tripathi M et al (2018) Identification of rocks and their quartz content in Amarkantak, India using ASTER TIR data. *Int Arch Photogramm* 42:5
- Gutman G, Huang C, Chander G et al (2013) Assessment of the NASA-USGS global land survey (GLS) datasets. *Remote Sens Environ* 134:249–265
- Harris JR, Grunsky EC (2015) Predictive lithological mapping of Canada's North using random forest classification applied to geophysical and geochemical data". *Comput Geosci* 80:9–25
- Ibrahim WS, Koichiro W, Yonezu K (2016) Structural and lithotectonic controls on Neoproterozoic base metal sulfide and gold mineralization in North Hamisana shear zone, South Eastern Desert, Egypt: The integrated field, structural, Landsat 7 ETM+ and ASTER data approach. *Ore Geol Rev* 79:62–77
- Kelman I, Field J, Suri K et al (2018) Disaster diplomacy in Jammu and Kashmir. *Int J Disast Risk Re* 31:1132–1140
- Kumar CSC, Oommen T, Guha A (2020) Automated lithological mapping by integrating spectral enhancement techniques and machine learning algorithms using AVIRIS-NG hyperspectral data in Gold-bearing granite-greenstone rocks in Hutti, India. *Int J Appl Earth Obs* 86:102006
- Lillesand TM, Kiefer RW, Chipman JW (2015) *Remote sensing and image interpretation*, 7th edn. John Wiley & Sons, NJ
- Liu P, Choo KKR, Wang L et al (2017) SVM or deep learning? A comparative study on remote sensing image classification. *Soft Comput* 21(23):7053–7065
- Lydekker R (1876) Notes on the geology of the Pir Panjal and neighboring districts. *Rec Geol Surv India* 9:155–183
- Notesco G, Kopačková V, Rojčík P, et al (2014) Mineral classification of land surface using multispectral LWIR and hyperspectral SWIR remote-sensing data. a case study over the Sokolov lignite open-pit mines, the Czech Republic. *Remote Sens* 6(8):7005–25
- Othman AA, Gloaguen R (2017) Integration of spectral, spatial and morphometric data into lithological mapping: a comparison of different machine learning algorithms in the Kurdistan Region, NE Iraq. *J Asian Earth Sci* 146:90–102
- Pedroni L (2003) Improved classification of Landsat Thematic Mapper data using modified prior probabilities in large and complex landscapes. *Int J Remote Sens* 24(1):91–113
- Pilgrim GE (1937) The Fossil Bovidae of India. *Pal Ind N S* 26(1):1–356
- Pour AB, Hashim M (2012) Identifying areas of high economic-potential copper mineralization using ASTER data in the Urumieh-Dokhtar Volcanic Belt. *Iran Adv Space Res* 49(4):753–769
- Pour AB, Hashim M (2012) The application of ASTER remote sensing data to porphyry copper and epithermal gold deposits. *Ore Geol Rev* 44:1–9
- Pour AB, Hashim M, Hong JK, Park Y (2017) Lithological and alteration mineral mapping in poorly exposed lithologies using Landsat-8 and ASTER satellite data: North-Eastern Graham Land, Antarctic Peninsula. *Ore Geol Rev* 108:112–133
- Pour AB, Park TYS, Park Y et al (2018) Application of multi-sensor satellite data for exploration of Zn–Pb sulfide mineralization in the Franklinian Basin. *North Greenland Remote Sens* 10(8):1186
- Pour AB, Park Y, Park TYS et al (2018) Regional geology mapping using satellite-based remote sensing approach in Northern Victoria Land Antarctica. *Polar Sci* 16:23–46
- Pour AB, Hashim M, Park Y, Hong JK (2018c) Mapping alteration mineral zones and lithological units in Antarctic regions using spectral bands of ASTER remote sensing data. *Geocarto Int* 33(12):1281–1306
- Pour AB, Park Y, Crispini L et al (2019) Mapping listvenite occurrences in the damage zones of Northern Victoria land, Antarctica using ASTER satellite remote sensing data. *Remote Sens* 11(12):1408
- Pour AB, Park TYS, Park Y et al (2019) Landsat-8, advanced spaceborne thermal emission and reflection radiometer, and WorldView-3 multispectral satellite imagery for prospecting copper-gold

- mineralization in the Northeastern Inglefield Mobile Belt (IMB). *Northwest Greenland Remote Sens* 11(20):2430
- Pour AB, Park Y, Park TY (2019) Evaluation of ICA and CEM algorithms with Landsat-8/ASTER data for geological mapping in inaccessible regions. *Geocarto Int* 34(7):785–816
- Rajan GR, Mayappan S (2019) Mapping of mineral resources and lithological units: a review of remote sensing techniques. *Int J Image Data Fusion* 10(2):79–106
- Safari M, Abbas M, Pour AB (2018) Application of Landsat-8 and ASTER satellite remote sensing data for porphyry copper exploration: a case study from Shahr-e-Babak, Kerman, south of Iran. *Geocarto Int* 33(11):1186–1201
- Sahoo S, Jha MK (2017) Pattern recognition in lithology classification: modeling using neural networks, self-organizing maps and genetic algorithms. *Hydrogeol J* 25(2):311–330
- Saporetta CM, da Fonseca LG, Pereira E (2019) A lithology identification approach based on machine learning with evolutionary parameter tuning. *Ieee Geosci Remote S* 16(12):1819–1823
- Sekandari, M., Masoumi, I., Beiranvand Pour, A., M Muslim, A., Rahmani, O., Hashim, M., ... & Aminpour, S. M. (2020). Application of Landsat-8, Sentinel-2, ASTER and WorldView-3 spectral imagery for exploration of carbonate-hosted Pb-Zn deposits in the Central Iranian Terrane (CIT). *Remote Sensing*, 12(8), 1239.
- Sheikhrasimi A, Pour AB, Pradhan B, Zoheir B (2019) Mapping hydrothermal alteration zones and lineaments associated with orogenic gold mineralization using ASTER data: a case study from the Sanandaj-Sirjan Zone. *Iran Adv Space Res* 63(10):3315–3332
- Takodjou W, Didero J, Pour AB et al (2020) Identifying high potential zones of gold mineralization in a sub-tropical region using Landsat-8 and ASTER remote sensing data: a case study of the Ngoura-Colomines goldfield, eastern Cameroon. *Ore Geol Rev* 122:103530
- Vapnik V (1995) *The nature of statistical learning theory*. Springer-Verlag 1:995
- Wang Z, Zuo R, Dong Y (2020) Mapping Himalayan leucogranites using a hybrid method of metric learning and support vector machine. *Comput Geosci* 138:104455
- Yang X (2011) Parameterizing support vector machines for land cover classification. *Photogramm Eng Rem S* 77(1):27–37
- Zhang T, Yi G, Li H et al (2016) Integrating data of ASTER and Landsat-8 OLI (AO) for hydrothermal alteration mineral mapping in duolong porphyry Cu-Au deposit, Tibetan Plateau. *China Remote Sens* 8(11):890
- Zuo R (2017) Machine learning of mineralization-related geochemical anomalies: a review of potential methods. *Nat Resour Res* 26(4):457–464
- Lillesand T, Kiefer RW, Chipman J (2014) *Remote sensing and image interpretation*. John Wiley & Sons

Publisher's note Springer Nature remains neutral with regard to jurisdictional claims in published maps and institutional affiliations.